arXiv:1511.01826v1 [cond-mat.mes-hall] 5 Nov 2015

High-conductive Organometallic Molecular Wires with Delocalized Electron Systems Strongly Coupled to Metal Electrodes

Florian Schwarz,[†] Georg Kastlunger,[‡] Franziska Lissel,[¶] Heike Riel,[†] Koushik Venkatesan,[¶] Heinz Berke,[¶] Robert Stadler,[‡] and Emanuel Lörtscher[*,†]

IBM Research - Zurich, Säumerstrasse 4, CH-8803 Rüschlikon, Switzerland, University of Vienna, Department of Physical Chemistry, Sensengasse 8/7, A-1090 Vienna, Austria, and Department of Chemistry, University of Zürich, Winterthurerstrasse 190, CH-8057 Zürich, Switzerland

Received November 6, 2015; E-mail: eml@zurich.ibm.com

Abstract *Besides active, functional molecular building blocks such as diodes or switches, passive components as, e.g., molecular wires, are required to realize molecular-scale electronics. Incorporating metal centers in the molecular backbone enables the molecular energy levels to be tuned in respect to the Fermi energy of the electrodes. Furthermore, by using more than one metal center and sp-bridging ligands, a strongly delocalized electron system is formed between these metallic "dopants", facilitating transport along the molecular backbone. Here, we study the influence of molecule–metal coupling on charge transport of dinuclear $X(PP)_2FeC_4Fe(PP)_2X$ molecular wires (PP = $Et_2PCH_2CH_2PEt_2$); X = CN (**1**), NCS (**2**), NCSe (**3**), C_4SnMe_3 (**4**) and C_2SnMe_3 (**5**)) under ultra-high vacuum and variable temperature conditions. In contrast to **1** which showed unstable junctions at very low conductance ($8.1 \cdot 10^{-7}$ G_0), **4** formed a Au-$C_4FeC_4FeC_4$-Au junction **4'** after $SnMe_3$ extrusion which revealed a conductance of $8.9 \cdot 10^{-3}$ G_0, three orders of magnitude higher than for **2** ($7.9 \cdot 10^{-6}$ G_0) and two orders of magnitude higher than for **3** ($3.8 \cdot 10^{-4}$ G_0). Density functional theory (DFT) confirmed the experimental trend in the conductance for the various anchoring motifs. The strong hybridization of molecular and metal states found in the C–Au coupling case enables the delocalized electronic system of the organometallic Fe_2 backbone to be extended over the molecule-metal interfaces to the metal electrodes to establish high-conductive molecular wires.*

KEYWORDS: Molecular wire, Single-molecule junctions, electronic transport, break-junctions, organometallic compounds, density functional theory

Molecular electronics aims at employing single molecules as functional building blocks in electronic circuits. Besides such active components which provide, e.g., current rectifying or switching properties, also passive components such as molecular wires are required for the realization of molecular-scale electronics. Generally, an ideal wire has lowest resistance with almost linear (ohmic) and length-independent (ballistic) transport properties. For molecular wires, the required high conductance can in principle be achieved if low injection barriers for charge-carriers are present at the molecule–metal interfaces, if molecular orbitals (MOs) are available close to the Fermi energy of the electrodes, and if a large degree of electronic conjugation across the backbone is present. Already the first task seems to be difficult to achieve as the most frequently used thiol anchoring [1,2] suffers from an electronically weak molecule–metal coupling. Additionally, multiple bonding sites available on the Au surface for the thiol bond give rise to alternating energy barriers for charge-carrier injection and result in large fluctuations in the transport properties. Therefore other anchoring schemes such as nitriles,[3] isocyanides,[4] amines,[5] and pyridines[6] were investigated. Dithiocarbamates[7] were demonstrated to increase the molecule–metal coupling compared to previously used single-bond anchors by at least one order of magnitude, and to simultaneously reduce fluctuations. The use of fullerenes as anchors[8–10] seems promising, because of the larger molecule–metal interface and the affinity of fullerenes for precious metals.[11] However, it turned out that the transport-limiting barriers shifted from the molecule–metal interfaces onto the molecular backbone, independently of the specific connection scheme to the fullerene.[12] In contrast to fullerenes with many, but weak sp^2 "bonds", the direct C–Au bond showed unprecedented high conductances for oligophenyls up to 0.9 G_0,[13] (for one phenyl ring) close to the theoretical maximum of 1 G_0 (with $G_0 = 2e^2/h \simeq 77\ \mu S$ the conductance quantum). The C–Au bond can be established either by extrusion of a trimethyltin moiety[13] or post deprotection of a trimethylsilyl moiety.[14] Currently, the direct C–electrode bond seems to be the most promising coupling scheme also for graphene electrodes[15,16] if polymerization via the free termini can be prevented.

Oligo(phenylene ethynylene)s (OPEs) were considered as one class of molecular wires as their conjugated backbone enables electron transport. In that respect, C–Au coupled OPEs are currently the highest conductive molecular wires[13,14] with an exponential conductance decay due to tunneling of approx. 1 order of magnitude per phenyl ring. Organometallic molecules[17] with incorporated metal centers form delocalized electron systems between two or more metal centers if appropriate ligand connections over unsaturated C bridges are chosen.[18] Furthermore, the MO levels can be tuned by the metal centers to better align with the Fermi energy of the leads. Motivated by this seminal idea, we have devised dinuclear Fe complexes[19] $X(PP)_2FeC_4Fe(PP)_2X$ consisting of a $[FeC_4Fe]$ backbone with highly delocalized electronic systems.[20] To investigate the effect of molecule–metal coupling on transport across the $[FeC_4Fe]$ backbone and its influence on the delocalized electronic system, we varied only the end groups coordinatively or covalently bonded to the $[FeC_4Fe]$ unit. All compounds can be considered as rigid-rod like structures with reduced conformational degrees of freedom. Fig. 1 C shows compounds **1**-**3** bound coordinatively via terminal CN, NCS and NCSe end-groups to Au, whereas the $SnMe_3$ end-capped compounds **4** and **5** (Fig. 1 D and 1 E) allow for different covalent bonding motifs (see SI), e.g. to form a direct covalent C–Au σ bond after extrusion of the $SnMe_3$ groups. The loss of the -$SnMe_3$ capping leads to a reduction in length of the anchoring groups and hence a shorter electrode–electrode distance for the resulting Au–molecule–Au system. The junction's length, however, determines also the direct electron-tunneling contribution between the electrodes, a non-negligible electron path parallel to the molecular-mediated one.[21] Accordingly, we couple C_4-$SnMe_3$

[†] IBM Research - Zurich

[‡] University of Vienna

[¶] University of Zurich

end groups to the Fe centers to achieve a length of 2.322 nm (distance between binding Au atoms) for the Au–**4′**–Au junction that is comparable to the one of the Au–**2**–Au (2.257 nm) and Au–**3**–Au (2.328 nm) junctions. In order to investigate length-effects on the molecule–electrode coupling, we have designed additionally compound **5** with shorter C_2-$SnMe_3$ end groups which forms the Au–**5′**–Au system with an electrode separation comparable to Au–**1**–Au. All [FeC_4Fe] compounds exhibit a high charge-delocalization between the two metal centers and can be oxidized or reduced reversibly in solution with up to three oxidation states at relatively low potentials (< 1.0 V).[19,20] (see SI).

To perform transport measurements, we use electron-beam-structured break-junctions (Fig. 1 B) that are mechanically actuated in a three-point bending mechanism (Fig. 1 A) operated in an ultra-high vacuum environment (UHV; pressure $p < 2 \cdot 10^{-9}$ mbar) and at variable temperature (10 K $< T <$ 300 K)[22] (see SI for details). Statistical data acquisition is performed by taking several hundred *I–V* characteristics curves in subsequent junction forming and breaking cycles.[22] Due to microscopic surface reconfigurations under the applied high fields and at elevated temperatures, only the opening data is considered. We first report on the transport properties of the compounds **1** - **5** taken at room-temperature (300 K). The measurement of compound **1** upon initial junction closing and subsequent opening and closing cycles under a fixed bias of 50 mV resulted in histograms that showed less distinct molecular signatures with a small conductance accumulation located at around $8.1 \cdot 10^{-7}$ G_0 (see SI). *I–V* data acquisition was not possible due to highly unstable junctions. In contrast, compounds **2**, **3**, **4** and **5** (transformed into **4′**, and **5′** respectively, upon attachment to the Au electrodes) gave reproducible *I–V* data upon repeated opening of the junction. The *I–V* data gathered was then mathematically derived to obtain (differential) conductance vs. voltage, G_{Diff}-*V*, curves. The entity of all these opening curves is displayed as a "density plot" in the left column of Fig. 2 with the color code representing the grade of accumulation. The data contains 1033 *I–V* characteristics taken for **2** (with a junction forming probability of 70%), 812 for **3** (70%), 636 **4** (98%), and 1929 for **5** (70%) as acquired during the identical measurement protocols of comparable cycle numbers. Based on the most probable accumulations, we have selected individual G_{Diff}-*V* characteristics (transparent blue curves) to display the functional behavior of individual curves. In addition, conductance histograms were constructed by taking the conductance data at ± 1.0 V from the opening curves (see SI for histograms extracted at other voltages and in absence of molecules). According to our measurement approach, the electrodes are brought in very close contact (approx. 0.1 nm) during every cycle, which results either in the formation of a direct Au–Au contact or multi-molecular junctions, depending primarily on the diffusion of surface Au atoms under the applied high field. Hence, the close-contact or high-conductance regime of (0.08 - 5.0) G_0 is therefore considered as not appropriately controlled at room temperature and henceforth indicated by a blue shaded background in the right column of Fig. 2.

Fig. 2A shows one broad and two narrow accumulations of G_{Diff}–*V* data for **2**. The corresponding conductance peaks in the histogram are located at 0.95 G_0, $1.5 \cdot 10^{-1}$ G_0 and $7.9 \cdot 10^{-6}$ G_0 as displayed in Fig. 2B. The first distribution represents Au–Au QPCs that are formed repeatedly during the measurement process. The most dominant and hence most probable distribution at $7.9 \cdot 10^{-6}$ G_0 is attributed to the formation of a Au–**2**–Au junction. In contrast, transport measurements of compound **3** reveal no clear accumulation in the *G–V* data (Fig. 2 C). Instead, a spread in the G_{Diff}–*V* data from 10^{-5} G_0 to 10^{-2} G_0 is found. The conductance histogram confirms this finding by a broad peak located at $3.8 \cdot 10^{-4}$ G_0. Much more distinct are the results for compound **4**, where three peaks are found at 0.86 G_0, $8.9 \cdot 10^{-3}$ G_0 and $9.6 \cdot 10^{-7}$ G_0 (Fig. 2 F), as could also be presumed from the *G–V* distribution (Fig. 2 E). Here, the first peak again originates from Au–Au metal junctions, whereas the second and third one are due to the formation of a Au–**4′**–Au junction. From the peak height, i.e. the relative occurrence, we preliminarily conclude that the most probable conductance is $7.9 \cdot 10^{-6}$ G_0 for **2**, $3.8 \cdot 10^{-4}$ G_0 for **3**, and $8.9 \cdot 10^{-3}$ G_0 for **4′** (all taken at 1 V). Besides the difference in the conductance maxima, also the spread in conductance differs clearly for the three different anchor groups being studied. For NCS and NCSe anchoring, the widths of the conductance histograms are approx. 3-4 orders of magnitude (e.g., $G_{3,high}/G_{3,low} = 4 \cdot 10^3$, estimated from the Full Width at Half Max (FWHM) of a Gaussian-like peak), and much less for direct C–Au anchoring, approx. 1-2 orders of magnitude ($G_{4,high}/G_{4,low}$ = 2.5·10). This smaller conductance variation is also found for the second C–Au coupled and shorter Au– **5′**–Au system as displayed in Fig. 2 G and H, which show an even higher conductance of $1.3 \cdot 10^{-2}$ G_0.

At room temperature, the MOs energy level are usually broadened and the Fermi energy of Au is broadened too, leading to rather monotonic and continuous *I–V* characteristics as displayed in Fig. 2 for all compounds. In contrast, the MOs usually become apparent in *G–V* characteristics at low temperatures, typically at less than 100 K, because of the reduced thermal broadening. We therefore investigated the transport properties exemplarily for **2** and **4′** at low temperatures (Fig. 3). The data exhibits a symmetric conductance gap of approx. 0.8 V for **2**, independent on the temperature (the data contains 120 *I–V* characteristics, 40 taken at 30 K, 50 K and 100 K each). In the low-voltage range up to ± 0.25 V, no MOs are available for electrons to tunnel through. At higher bias, however, the current starts to increase as frontier MOs (according to DFT the HOMO, see below) get into resonance. As can be seen best in the *G-V* representation, where the resonant MOs are represented by peaks, they are located at -0.85 V, -0.39 V, 0.39 V, and 0.87 V. They are spaced symmetrically with respect to bias polarity, as it is expected for symmetric molecules and symmetric coupling. In addition to the conductance gap and the appearance of discrete MO resonances in **2**, many *I–V* characteristics with the appearance of hysteretic conductance switching are found (see SI). All these findings differ strongly to those for compound **4′**, where only monotonous curves without a conductance gap were recorded at low temperatures. Fig. 3 shows 100 *I–V* (C), and G_{Diff}-*V* (D) characteristics of **4′**, taken at 50 K (similar data for 30 K and 100 K): Besides the absence of discrete MO peaks, the transport properties are more linear and the current levels are 3 to 4 orders of magnitude higher.

To study the MO alignment and landscape, we performed Density Functional Theory (DFT) calculations with a PBE XC-functional within a NEGF-DFT framework[23–25] using the GPAW-code[26,27] to compute transmission probabilities, $T(E)$. In order to account for selfinteraction errors and image charge effects present in DFT with local XC-functionals we applied a scissor operator (SO), according to Quek et al.,[5] to the weaker coupled molecules **1** to **3** (see SI). All DFT calculations were carried out without treating spin polarisation as a degree of freedom since previous tests on Fe complexes with the same ligand field revealed the low spin configuration to be the ground state. The results of the DFT calculations for the transmission functions T(E) and eigenenergies of the respective orbitals HOMO and HOMO-1 relative to E_F are presented in Fig. 4A and B for the compounds **1** to **5′**. Fig. 4C displays calculated *I–V* curves that were obtained from the transmission functions T(E) in a rigid band approximation where the bias dependence of T(E) is disregarded, as $I = \frac{2e}{h} \int_{-\infty}^{+\infty} T(E)[f_1(E) - f_2(E)]dE$ with $f_{1,2}$ as the respective Fermi functions for the two electrodes at 50 K and their chemical potentials shifted by $\pm eV/2$. The figure illustrates

the relation between the energetic position of those two MOs and the characteristic double peaks in the transmission. Furthermore it shows the spatial distribution of these two MOs. Both the eigenvalues and the shape of the relevant MOs are similar for all systems, consisting of π-orbitals delocalized over the entire molecular backbone and containing equal amounts of both Fe d-states. For each system, the HOMO and HOMO-1 differ only in the sense that they are rotated by 90° to each other, which might indicate an energetic degeneracy of the two states. However the rotational symmetry is slightly disturbed by the $(PP)_2$ ligands on the Fe centers explaining the small energetic splitting and therefore the appearance of a double-peak structure in the transmission function. The conductance at zero bias, which is given in Fig. 5 B) and compared to experimental findings, is mainly influenced by the tails of the HOMO and HOMO-1 peaks, leading to quite different values among the compounds investigated. Although the metal–molecule coupling is quite high for all anchor groups, the two C–Au end groups surpass the others with rather strong covalent bonding, which leads not only to broad peaks in the transmission function, but also to a more distinct energy shift of the peaks towards E_F caused by hybridization of the MOs and the lead bands. It can be seen that the aligned MO eigenenergies for the different anchor schemes are rather similar with the exception of compound 1, thereby ruling out structural variations in the charge transfer[28–30] as a possible source for the differences in the transmission peak energies for compound 2-5', and leaving only variations in the hybridization strengths as explanation. As a consequence, even the rather long C_4 anchors of **4′** lead to a higher conductance than the coordinatively bonding end groups CN, NCS and NCSe, although the rate of coherent tunneling decreases rapidly with the Au–Au distance in a molecular junction. Similar to the arguments for the superior conductance provided by the C–metal end groups, also the conductance ordering for the thiol and selenium anchors can be rationalized by the fact that the electronic coupling strength of Se–Au exceeds that of S–Au[31,32] due to a larger overlap of the wavefunctions. We start the discussion of experimental and theoretical findings with compound **1**. The presence of only weak and rather unlikely molecular signatures (of $8.1 \cdot 10^{-7}$ G_0 at 50 mV bias) in the low-bias transport data of compound **1**, can have several reasons: First, the conductance of compound **1** is either below our experimental resolution ($\ll 1.0 \cdot 10^{-8}$ G_0), or, second, the CN binding to Au is weak and the resulting Au-**1**-Au junction is not stable under high bias, or, third, the bulky ligands prevent the terminals to bind to the Au electrodes due to the short distance to the Fe center. For compounds **2**, **3**, **4′** and **5′**, the room-temperature experiments worked reproducibly and the conductance data displayed in Fig. 2 shows values that range from slightly larger than 1 G_0 down to 10^{-8} G_0. It is hence ensured that all possible configurations during the junction forming and breaking procedure, from fully open Au contacts to Au–molecule–Au junctions and direct Au–Au QPCs were probed. The QPC peak at 1 G_0 confirms that the electrodes completely touched (at least in some of the cycles) in the required gentle way, i.e., not fusing the contact entirely. The data gathered, noticeably, represents conductances of all possible electrode distances. In case of **2**, a broad peak with a maximum at $7.9 \cdot 10^{-6}$ G_0 is formed. The fluctuations giving rise to this broad peak are typically generated by variations in the S–Au bond as multiple bonding sites (top, hollow, bridge etc.) are available on the Au surface. An even wider peak is found for the Se–Au bond of compound **3**, indicating multiple bonding sites with fast binding kinetics and low transition states for site exchange that do not necessarily need thermodynamic activation for the weaker Se–Au (binding energy of 0.516 eV compared to 0.669 eV for S–Au) bond. For both C–Au coupled compounds **4′** and **5′**, much narrower conductance accumulations are found. In the DFT calculations, the top position was identified to be the energetically most stable configuration. As a consequence, the C–Au anchors of compounds **4′** and **5′** are supposed to be in their equilibrium bonding-site configuration even under mechanical manipulation of the junction, which results in narrow conductance histogram peaks. In the transport data of compound **4′** (and weaker also in case of **5′**), a second, broader but smaller peak compared to the main peak at $8.9 \cdot 10^{-3}$ G_0 is found at $9.6 \cdot 10^{-7}$ G_0. The appearance of a second peak at a lower average conductance for **4′** (and similar also for **5′**) is presumed to originate from the various bonding scenarios of the C end group: Incomplete cleavage of the $SnMe_3$ capping, formation of chemically reasonable alkynyl vinylidene trimethyltin species [(-C≡C)($SnMe_3$)C=C)] upon binding to the gold electrode resulting in the formation of a carbene type bond to the Au electrode ([Au-C_4FeC_4Fe-C≡C($SnMe_3$)C=C=Au] = Au–**4″**–Au) (see SI), transport through one of the bis(diethylphosphino)ethane ligands (as one or two arms of the phosphine ligands could lift-off to form Fe-PCH_2-CH_2-P → Au) and non-cleaved end groups cappings. Alternatively in our understanding, also reductive C–C coupling forming a dimerized Au–$C_4FeC_4FeC_8FeC_4FeC_4$–Au (Au–**4′**-**4′**–Au) junctions (similarly for **5′**) can occur. As such details of the junction configuration are experimentally not directly accessible, the conductances of the Au-**4′**-**4′**-Au and Au-**5′**-**5′**-Au dimer junctions and the vinylidene-coupling case were exemplarily calculated (see SI). A conductance of $1.05 \cdot 10^{-5}$ G_0 was found for the dimer junction Au–**4′**-**4′**–Au. In the transmission function of the dimer, the slope at the Fermi level is relatively high, which means that a small energy shift of 0.1 eV would result in a lower calculated conductance. This notion is in agreement with the experimental finding as such a small shift in energy could also be argued to arise from deficiencies of DFT such as gap underestimation. Due to the good agreement between DFT and experiments for both the 'monomer' and the 'dimer' compounds, we conclude that spontaneous dimerization is most likely the origin for the low-conductance peaks of compounds **4** (and also **5**), in agreement with the observation of dimerization in $SnMe_3$-capped oligophenyls with C–Au anchors.[13] A dimerization explains further why the contacting traces for molecular signatures are 5-7 times longer for the low-conductance I-Vs compared to the high-conductance *I-V*s (see SI).

When comparing the main peaks in the conductance data at high bias (1.0 V) or low bias (0.2 V, see SI) of **2**, **3**, **4′** and **5′** measured at 300 K, a good qualitative agreement with DFT at zero-bias is found as directly compared in Fig. 5 B). The zero-bias conductance according to DFT and the low-bias current in the experiments are both much higher for **4′** or **5′** than for **2** and **3**, which indicates that the LDOS is much higher for the C–Au coupled systems than that of the others. The orbital distribution indicates that a strong hybridization of MOs and metal states takes places at the molecule–metal interfaces in the C–Au coupled system as evidenced by the difference in the HOMO's amplitude on the bonding site as obtained from DFT data highlighted by circles in Fig. 5 D. This hybridization shifts HOMO and HOMO-1 closer to E_F, leading to an earlier onset in electron transport as evidenced by the low-temperature transport properties where the conductance gap has even vanished (Fig. 3). Injection barriers estimated from minima in the transition-voltage-spectroscopy representation ($\ln(I/V^2)$–(1/V); see SI) reveal a similar barrier height of (1.75 ± 0.3) 1/V for **4′** and (1.85 ± 0.3) 1/V for **5′** in contrast to (4.2 ± 1.5) 1/V for **3**, and (5.5 ± 1.5) 1/V for **2** at 300 K. The strong hybridization of metal and molecular states established by the C–Au coupling might further be the reason why the hysteretic switching behavior found at low temperatures for the weakly coupled compound **2** (see SI) was not revealed in the strong C–Au coupled compound **4′** as the MOs are more pinned and intrinsic functionality might be prohibited. The energetic positions of

the frontier MOs found for compound **2** at around ± 0.4 V at low temperatures are in quantitative agreement with the energetic difference between HOMO and E_F calculated by DFT to be around 0.25 eV - 0.30 eV as illustrated in Fig. 4B. These values are around 100 meV smaller than the MO energies in Fig. 3B which is due to the mean field character of DFT with semi-local exchange correlation functionals which do not capture many body effects.[33,34]

Compared with trimethylsilyl-[14] or trimethyltin-capped oligophenyls with a direct Au–benzene attachment,[35] the conductance of compound **4′** is more than ten-fold higher if similar wire lengths, *l*, (approx. 2 nm) are taken into account. When comparing with organometallic ruthenium(II) bis(σ-arylacetylide) complexes with SCN-Au coupling,[36,37] the conductance of **4′** is more than one order of magnitude higher. For trimethyltin-capped polyphenyls with additional carbon atoms in the Au–C–benzene bonds,[13] a conductance of $1.4 \cdot 10^{-2}$ G_0 was found for 4 phenyl units, similarly high as the one of compound **4′**. When taking the dimer system Au–**4′**–**4′**–Au into account, we can create a preliminary length-dependence for the conductance decrease with wire length ($G \propto e^{-\beta' l}$) of the Fe-based organometallic wires to compare with state-of-the-art molecular wires (see SI). The decay constants of β = 4.4 nm^{-1} (determined by experimental values at 200 mV or 1.0 V) and β = 3.5 nm^{-1} (DFT at zero bias) are both higher than for the organometallic ruthenium(II) bis(σ-arylacetylide) complexes[36,37] (β = 1.02 - 1.64 nm^{-1}) or purely organic oligothiophenes[38] (β = 1.0 nm^{-1}) with lowest decay constants reported so far. The values estimated and calculated are closer to decay constants for phenyls coupled via C–Au[13] (β = 4.0 - 6.0 nm^{-1}). A full experimental study of oligomeric organometallic molecules with 1 to 4 repeating Fe units, however, has to confirm this preliminary estimation.

In summary, we have theoretically and experimentally investigated the influence of molecule–metal coupling on the electron transport properties of dinuclear Fe complexes. We varied the molecule–metal coupling systematically by using different anchoring schemes, such as CN, NCS, NCSe, C_2SnMe_3 and C_4SnMe_3 with the latter two end groups leading to a direct C–Au bond after $SnMe_3$ extrusion. Whereas the CN termination did not result in stable junctions, all other end groups yielded reproducible transport junctions that enabled the determination of the room-temperature coupling strengths, which follow the order $\Gamma_{NCS-Au} < \Gamma_{NCSe-Au} < \Gamma_{C_4-Au} < \Gamma_{C_2-Au}$, in qualitative agreement with DFT calculations. Moreover, the reproducible binding of the C-Au motif upon extrusion or migration of the $SnMe_3$ end-group was demonstrated to occur also at low temperatures (50 K), leading to the formation of high-conductive molecular wires. Overall, the class of organometallic compounds with delocalized electron systems between two and more metal centers is a promising concept to achieve long and highly conductive wires due to an extension of the electronic system of the [FeC_4Fe] unit over the molecule–metal interfaces to the electrodes by strong hybridization. Beyond that, organometallic compounds are an attractive framework for the integration of intrinsic functionality for future applications such as redox activity for conductance switching and memory application.

ASSOCIATED CONTENT

Supporting Information on the synthesis of the compounds, the experimental setup, control measurements, histograms at other voltages and additional DFT calculations. This material is available free of charge via the Internet at http://pubs.acs.org.

AUTHOR INFORMATION

Corresponding Author for chemistry: hberke@chem.uzh.ch (H.B.), venkatesan.koushik@chem.uzh.ch (K.V.); DFT calculations: robert.stadler@univie.ac.at (R.S.); experiments: eml@zurich.ibm.com (E.L.)

NOTES

The authors declare no competing financial interest.

ACKNOWLEDGMENTS

We are grateful to B. Gotsmann, V. Schmidt, and W. Riess for scientific discussions, and to M. Tschudy, U. Drechsler and Ch. Rettner for technical assistance. Funding from the National Research Programme "Smart Materials" (NRP 62, grant 406240-126142) of the Swiss National Science Foundation (SNSF) and the University of Zürich is gratefully acknowledged. G.K. and R.S. are currently supported by the Austrian Science Fund FWF, project Nr. P22548 and are deeply indebted to the Vienna Scientific Cluster VSC, on whose computing facilities all DFT calculations have been performed (project Nr. 70174).

References

(1) Bumm, L. A.; Arnold, J. J.; Cygan, M. T.; Dunbar, T. D.; Burgin, T. P.; Jones II, L.; Allara, D. L.; Tour, J. M.; Weiss, P. S. *Science* **1996**, *271*, 1705–1707.
(2) Reed, M. A.; Zhou, C.; Muller, C. J.; Burgin, T. P.; Tour, J. M. *Science* **1997**, *278*, 252–254.
(3) Metzger, R. M.; Chen, B.; Höpfner, U.; Lakshmikantham, M. V.; Vuillaume, D.; Kawai, T.; Wu, X.; Tachibana, H.; Hughes, T. V.; Sakurai, H.; Baldwin, J. W.; Hosch, C.; Cava, M. P.; Brehmer, L.; Ashwell, G. J. *J. Am. Chem. Soc.* **1997**, *119*, 10455–10466.
(4) Chen, J.; Calvet, L. C.; Reed, M. A.; Carr, D. W.; Grubisha, D. S.; Bennett, D. W. *Chem. Phys. Lett.* **1999**, *313*, 741–748.
(5) Quek, S. Y.; Neaton, J. B.; Hybertsen, M. S.; Venkataraman, L.; Choi, C. H.; Louie, S. G. *Nano Lett.* **2007**, *7*, 3477–3482.
(6) Kamenetska, M.; Su, Y. Q.; Whalley, A. C.; Steigerwald, M. L.; Choi, H. J.; Louie, S. G.; Nuckolls, C.; Hybertsen, M. S.; Neaton, J. B.; Venkataraman, L. *J. Am. Chem. Soc.* **2010**, *132*, 6817–6821.
(7) von Wrochem, F.; Gao, D.; Scholz, F.; Nothofer, H.-G.; Nelles, G.; Wessels, J. M. *Nature Nanotech.* **2010**, *5*, 618–623.
(8) Martin, C. A.; Ding, D.; Sørensen, J. K.; Bjørnholm, T.; van Ruitenbeek, J. M.; van der Zant, H. S. J. *J. Am. Chem. Soc.* **2008**, *130*, 13198–13199.
(9) Fock, J.; Sørensen, J. K.; Lörtscher, E.; Vosch, T.; Martin, C. A.; Riel, H.; Kilså, K.; T., B.; van der Zant, H. *Phys. Chem. Chem. Phys.* **2011**, *13*, 14325–14332.
(10) Lörtscher, E.; Geskin, V.; Gotsmann, B.; Fock, J.; Sørensen, J. K.; Bjørnholm, T.; Cornil, J.; van der Zant, H. S. J.; Riel, H. *Small* **2013**, *9*, 209–214.
(11) Joachim, C.; Gimzewski, J. K.; Schlittler, R.; Chavy, C. *Phys. Rev. Lett.* **1995**, *74*, 2102–2105.
(12) Leary, E.; Gonzalez, T. M.; van der Pol, C.; Bryce, M. R.; Filippone, S.; Martin, N.; Rubio Bollinger, G.; Agraï, N. *Nano Lett.* **2011**, *11*, 2236–2241.
(13) Chen, W.; Widawsky, J. R.; Vazquez, H.; Schneebeli, S. T.; Hybertsen, M. S.; Breslow, R.; Venkataraman, L. *J. Am. Chem. Soc.* **2011**, *133*, 17160–17163.
(14) Hong, W.; Li, H.; Liu, S.-H.; Fu, Y.; Li, J.; Kaliginedi, V.; Decurtins, S.; Wandlowski, T. *J. Am. Chem. Soc.* **2012**, *134*, 19425–19431.
(15) Cao, Y.; Dong, S.; Liu, S.; Liu, Z.; Guo, X. *Angew. Chem. Int. Ed.* **2013**, *52*, 3906–3910.
(16) Lörtscher, E. *Nature Nanotech.* **2013**, *8*, 381–384.
(17) Ceccon, A.; Santi, S.; Orian, L.; Bisello, A. *Coord. Chem. Rev.* **2004**, *248*, 683–724.
(18) Pevny, F.; Di Piazza, E.; Norel, L.; Drescher, M.; Winter, R. F.; Rigaut, S. *Organometallics* **2010**, *29*, 5912.
(19) Lissel, F.; Schwarz, F.; Blaque, O.; Riel, H.; Lörtscher, E.; Venkatesan, K.; Berke, H. *Submitted* **2014**,
(20) Lissel, F.; Fox, T.; Blacque, O.; Polit, W.; Winter, R. F.; Venkatesan, K.; Berke, H. *J. Am. Chem* **2013**, *135*, 4051–4060.
(21) Gotsmann, B.; Riel, H.; Lörtscher, E. *Phys. Rev. B* **2011**, *84*, 205408.
(22) Lörtscher, E.; Weber, H. B.; Riel, H. *Phys. Rev. Lett.* **2007**, *98*, 176807.
(23) Brandbyge, M.; Mozos, J.-L.; Taylor, J.; Stokbro, K. *Phys. Rev. B* **2002**, *65*, 165401.
(24) Xue, Y.; Datta, S.; Ratner, M. A. *Chem. Phys.* **2002**, *281*, 151.
(25) Rocha, A. R.; Garcia-Suarez, V. M.; Bailey, S. W.; Lambert, C. J.; Ferrer, J.; Sanvito, S. *Nature Mater.* **2005**, *4*, 335.
(26) Mortensen, J. J.; Hansen, L. B.; Jacobsen, K. W. *Phys. Rev. B* **2005**, *71*, 035109.
(27) Enkovaara, J.; Rostgaard, C.; Mortensen, J. J.; Chen, J.; Dulak, M.; Ferrighi, L.; Gavnholt, J.; Glinsvad, C.; Haikola, V.; Hansen, H. A.; Kristoffersen, H.; Kuisma, M.; Larsen, A. H.; Lehtovaara, L. *J. Phys.: Conf. Ser.* **2010**, *22*, 253202.

(28) Stadler, R.; Jacobsen, K. W. *Phys. Rev. B* **2006**, *74*, 161405.
(29) Stadler, R. *J. Phys.: Conf. Ser.* **2006**, *61*, 1097–1101.
(30) Stadler, R. *Phys. Rev. B* **2010**, *81*, 16429.
(31) Patrone, L.; Palacin, S.; Bourgoin, J.-P.; Lagoute, J.; Zambelli, T.; Gauthier, S. *Chem. Phys.* **2002**, *281*, 325–332.
(32) Yaliraki, S. N.; Kemp, M.; Ratner, M. A. *J. Am. Chem. Soc.* **1999**, *121*, 3428–3434.
(33) Geskin, V.; Stalder, R.; Cornil, J. *Phys. Rev. B* **2009**, *80*, 085411.
(34) Stadler, R.; Cornil, J.; Geskin, V. *J. Chem. Phys.* **2012**, *137*, 074110.
(35) Chen, Z. L.; Skouta, R.; Vazquez, H.; Widawsky, J. R.; Schneebeli, S.; Chen, W.; Hybertsen, M. S.; Breslow, R.; Venkataraman, L. *Nat. Nanotech.* **2011**, *6*, 353–357.
(36) Kim, B.; Beebe, J. M.; Olivier, C.; Rigaut, S.; Touchard, D.; Kushmerick, J. G.; Zhu, X.-Y.; Frisbie, C. D. *J. Phys. Chem. C* **2007**, *111*, 7521–7526.
(37) Luo, L.; Benameur, A.; Brignou, P.; Choi, S. H.; Rigaut, S.; Frisbie, C. D. *J. Phys. Chem. C* **2011**, *115*, 19955–19961.
(38) Yamada, R.; Kumazawa, H.; Noutoshi, T.; Tanaka, S.; Tada, H. *Nano Lett.* **2008**, *8*, 1237–1240.

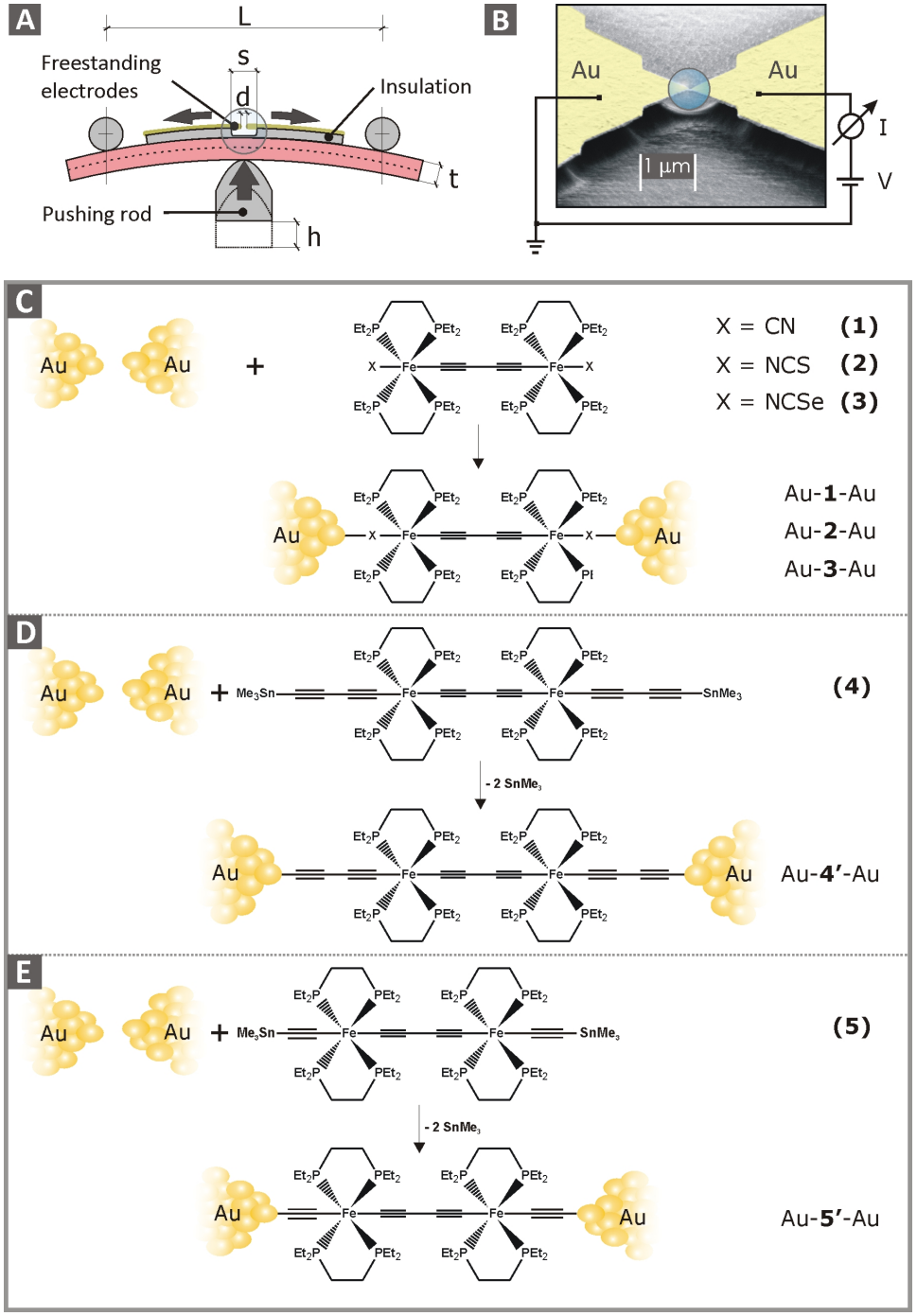

Figure 1. A) Operation principle of a mechanically controllable break-junction. B) Scanning electron microscope (SEM) image of a micro-structured sample. C) Compounds **1** - **3** with corresponding reaction schemes upon coupling to Au electrodes. In contrast to compounds **1** - **3**, the $SnMe_3$ end groups of **4** and **5** cleave off and direct C–Au bonds are formed yielding the Au–**4′**–Au (D) and the Au–**5′**–Au junction (E), respectively.

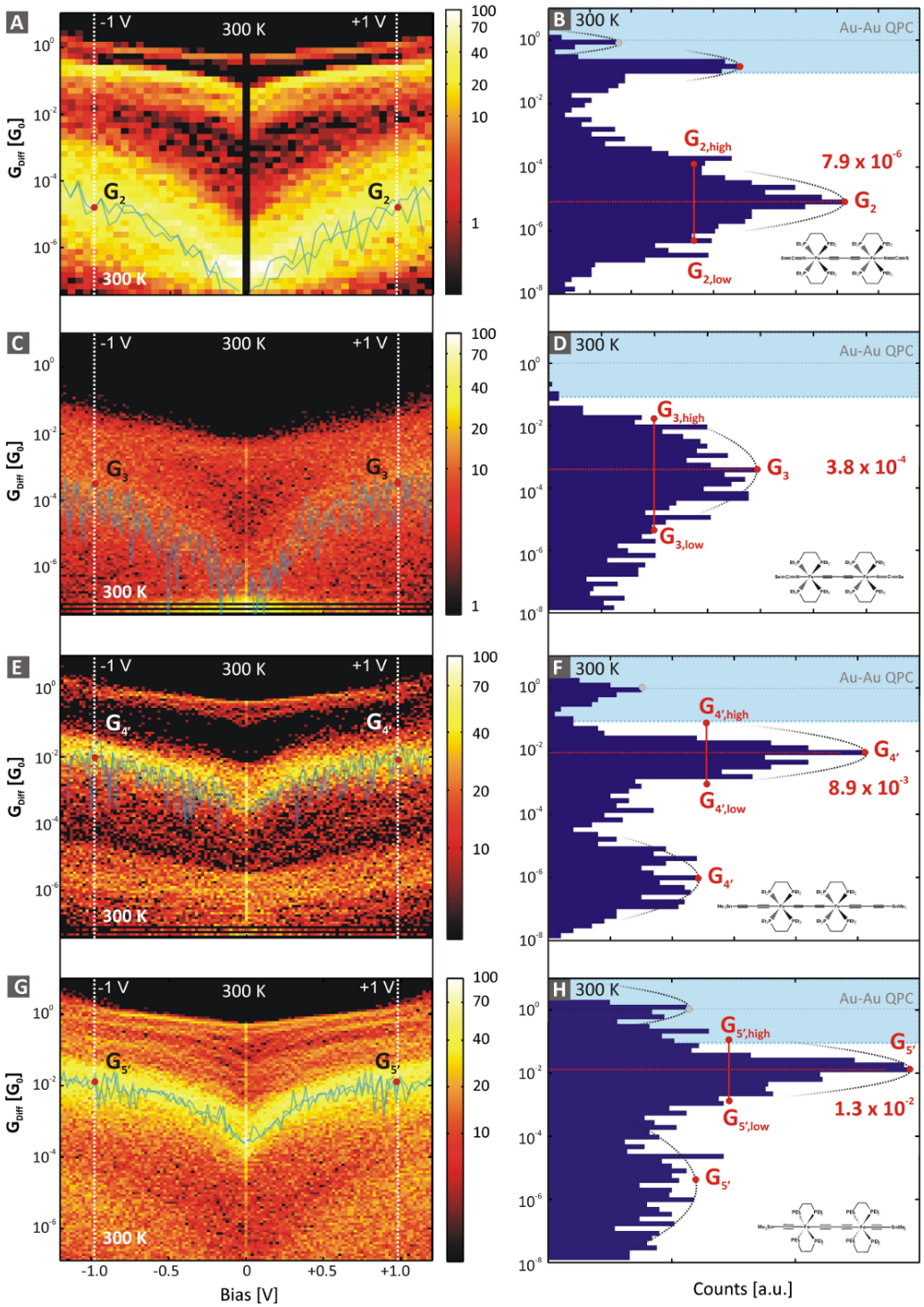

Figure 2. Density plots of the differential conductance, vs. voltage, G_{Diff}–V, characteristics acquired upon repeated opening of the junction at 300 K for compounds **2** (A), **3** (C), **4′** (E), and **5′** (G) upon opening of the junction at 300 K. Individual G_{Diff}–V curves (raw data) are plotted in transparent blue to display the functional behavior of an individual curve. Corresponding conductance histograms extracted at ± 1.0 V are displayed for **2** (B), **3** (D), **4′** (F), and **5′** (H). The blue area signals the smallest electrode separations that can either lead to a direct Au-Au contact (and hence a QPC) or multi-molecule junctions. The maximum conductance accumulation is labelled in red with a FWHM estimation for the peak width.

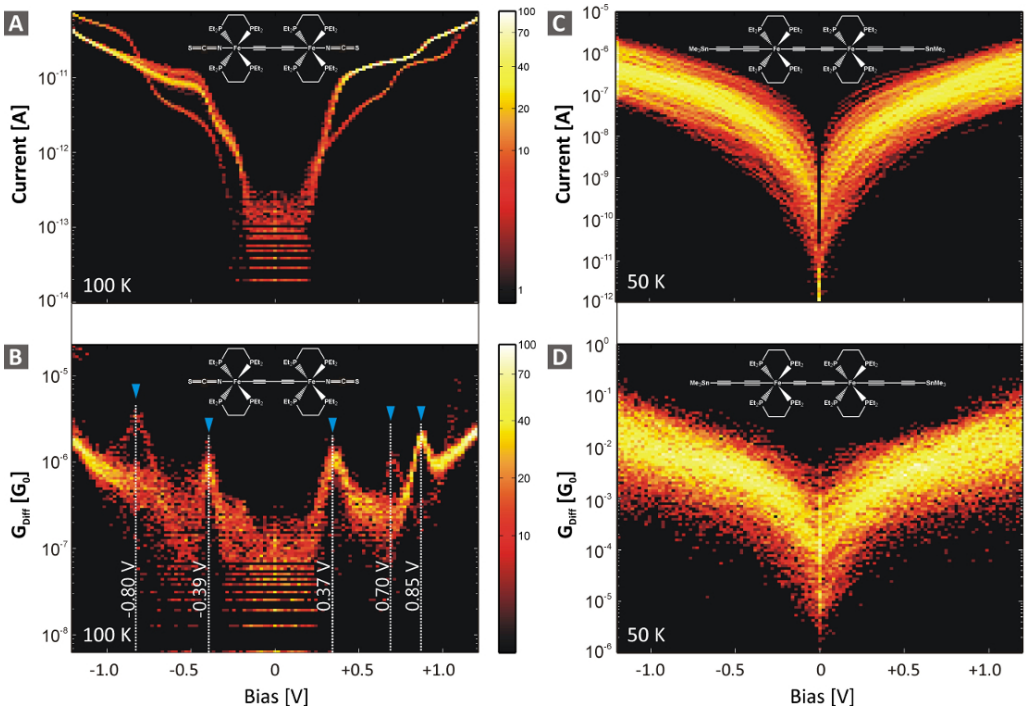

Figure 3. *I–V* and G_{Diff}-*V* characteristics taken at low temperatures upon repeated opening the junction for **2** in A) and B), and for **4′** in C) and D), respectively. For **2**, resonant transport through molecular orbitals gives rise to conductance peaks at specific voltages that are symmetric in respect to bias. In contrast, **4′** reveals exclusively monotonic curves without the appearance of discrete MOs. Furthermore, current levels are 3 orders of magnitude higher for the high-bias regime of **4′**, and 4 orders of magnitude higher for the low-bias regime due to the appearance of a conductance gap of approx. 0.8 V for **2**.

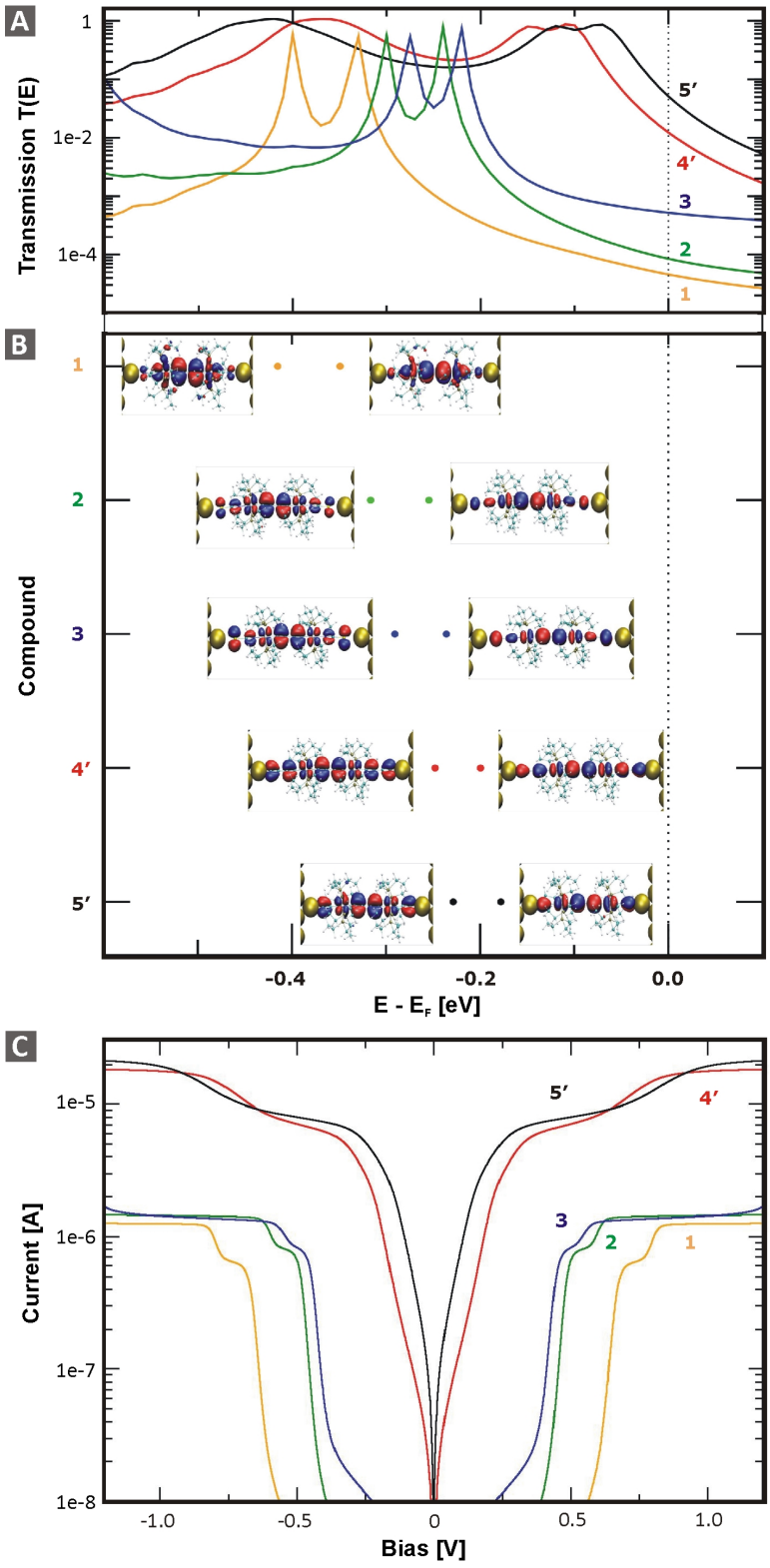

Figure 4. A) Transmission functions for compounds **1** to **5′** as calculated by DFT (color coding according to B)). B) Energetic positions of the HOMO and HOMO-1 of compounds **1** to **5′** represented as dots with different colors for the different systems with respect to the Fermi energy of the electrodes. Also given are the respective spatial distributions of these HOMO and HOMO-1. The slight shift of the transmission peaks toward the electrode Fermi Level results from the hybridization of the MOs with the gold bands, which is removed by the subdiagonalization process used to obtain the molecular states in the composite system. C) Calculated *I*–*V* curves obtained from the transmission functions T(E) in a rigid band approximation where the bias dependence of T(E) is disregarded.

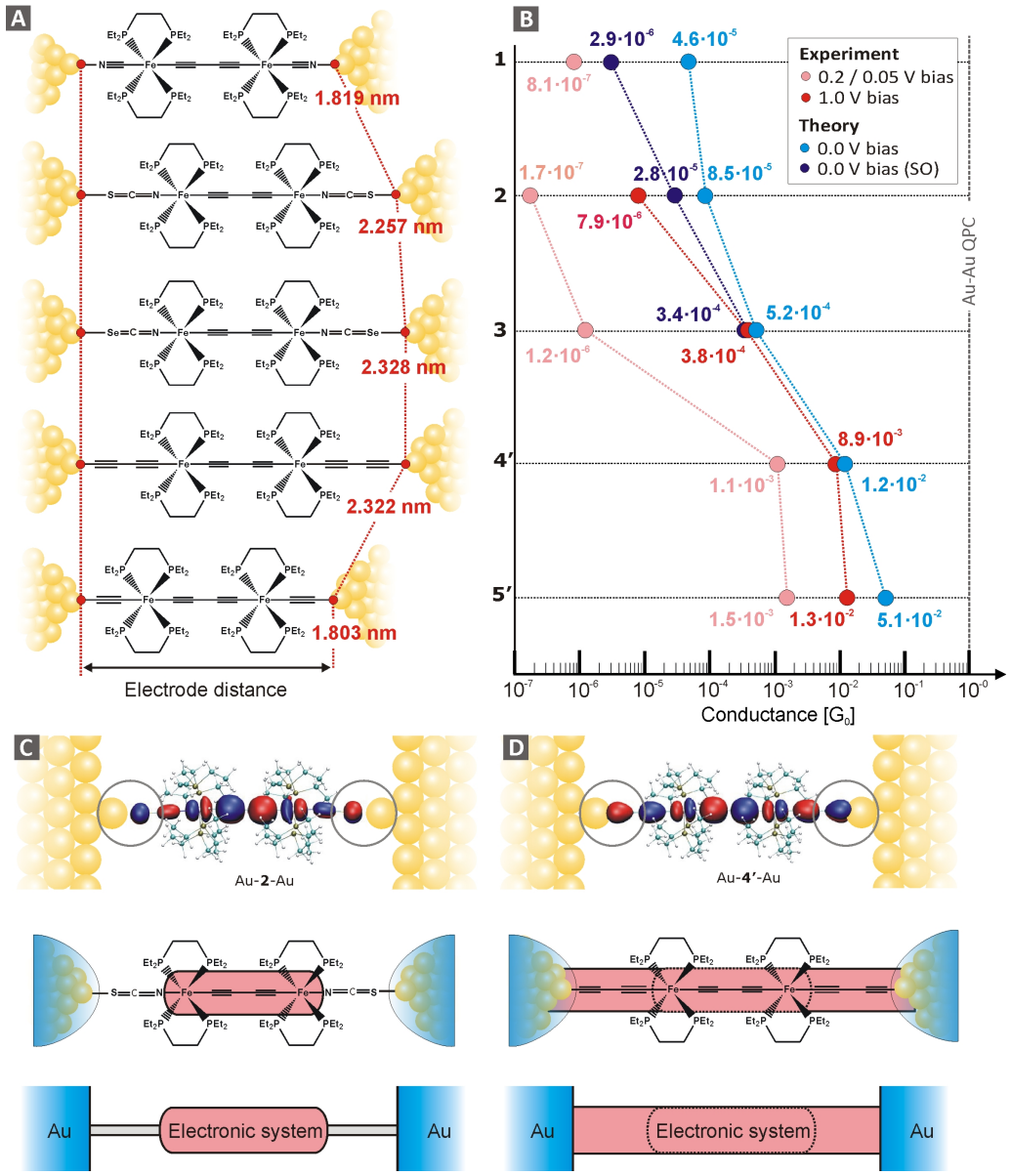

Figure 5. A) Calculated Au–Au distances of the resulting molecular junctions for compounds **1** to **5′**. B) Comparison of conductances for all compounds determined by experiment (300 K; 200 mV, 1.0 V) and DFT (0 K, zero bias, with and without scissor operator (SO) corrections). The experimental data point for **1** was achieved by low-bias measurements (50 mV). Schematic representation of the Au-**2**-Au (C) and the Au-**4′**-Au junction (D). The strong hybridization of metal and molecular states in the case of Au-**4′**-Au as evidenced by the difference in the HOMO's amplitude on the bonding site as obtained from DFT (gray circles), leads to the formation of a strong molecule–metal bond and enables to extend the delocalized electronic system between the two Fe centers over the molecule–electrode interfaces, in contrast to the weakly bonded Au-**2**-Au system.